

Dark-field Chest X-ray Imaging for the Assessment of COVID-19 Pneumonia

Manuela Frank (✉ manuela.frank@tum.de)

Technical University of Munich <https://orcid.org/0000-0001-5642-0694>

Florian Gassert

Klinikum rechts der Isar, Technical University of Munich

Theresa Urban

Technical University of Munich

Konstantin Willer

Technical University of Munich

Wolfgang Noichl

Technical University of Munich

Rafael Schick

Technical University of Munich

Manuel Schultheiß

Technical University of Munich <https://orcid.org/0000-0002-4261-5420>

Manuel Viermetz

Technical University of Munich <https://orcid.org/0000-0002-7332-1900>

Bernhard Gleich

Technische Universität München

Fabio De Marco

Technical University of Munich

Julia Herzen

Technische Universität München <https://orcid.org/0000-0002-9456-1591>

Thomas Koehler

Philips GmbH Innovative Technologies <https://orcid.org/0000-0002-1986-0057>

Klaus Juergen Engel

Philips Research

Bernhard Renger

Technische Universität München

Felix Gassert

Klinikum rechts der Isar, Technical University of Munich

Andreas Sauter

Klinikum rechts der Isar <https://orcid.org/0000-0003-4394-862X>

Alexander Fingerle

Klinikum rechts der Isar, Technical University of Munich

Bernhard Haller

Technical University of Munich <https://orcid.org/0000-0002-9723-393X>

Marcus Makowski

Klinikum rechts der Isar, Technical University of Munich

Daniela Pfeiffer

Technical University Munich

Franz Pfeiffer

Technical University Munich <https://orcid.org/0000-0001-6665-4363>

Article

Keywords:

Posted Date: April 7th, 2022

DOI: <https://doi.org/10.21203/rs.3.rs-1427370/v1>

License:  This work is licensed under a Creative Commons Attribution 4.0 International License.

[Read Full License](#)

Additional Declarations: **Yes** there is potential Competing Interest. T.K. and K.J.E. are employees of Philips GmbH Innovative Technologies. The remaining authors declare no competing interests.

Version of Record: A version of this preprint was published at Communications Medicine on November 21st, 2022. See the published version at <https://doi.org/10.1038/s43856-022-00215-3>.

Dark-field Chest X-ray Imaging for the Assessment of COVID-19-Pneumonia

Authors: Manuela Frank^{1,2,3*†}, Florian T. Gassert^{3†}, Theresa Urban^{1,2,3}, Konstantin Willer^{1,2,3}, Wolfgang Noichl^{1,2}, Rafael Schick^{1,2,3}, Manuel Schultheiss^{1,2,3}, Manuel Viermetz^{1,2}, Bernhard Gleich², Fabio De Marco^{1,2}, Julia Herzen^{1,2}, Thomas Koehler^{4,5}, Klaus Jürgen Engel⁴, Bernhard Renger³, Felix G. Gassert³, Andreas Sauter³, Alexander A. Fingerle³, Bernhard Haller⁶, Marcus R. Makowski³, Daniela Pfeiffer^{3,5}, Franz Pfeiffer^{1,2,3,5}

Affiliations:

¹Chair of Biomedical Physics, Department of Physics, School of Natural Sciences, Technical University of Munich, 85748 Garching, Germany.

²Munich Institute of Biomedical Engineering, Technical University of Munich, 85748 Garching, Germany.

³Department of Diagnostic and Interventional Radiology, School of Medicine & Klinikum rechts der Isar, Technical University of Munich, 81675 München, Germany.

⁴Philips Research Hamburg, Germany.

⁵Institute for Advanced Study, Technical University of Munich, 85748 Garching, Germany.

⁶Institute of AI and Informatics in Medicine, School of Medicine & Klinikum rechts der Isar, Technical University of Munich, 81675 München, Germany.

*Correspondence to: manuela.frank@tum.de

†These authors contributed equally to this work.

Abstract/Summary

Medical imaging is performed in daily clinical routine for the assessment of pulmonary involvement in patients infected with COVID-19. As conventional (attenuation-based) chest radiography provides only a low sensitivity for COVID-19-pneumonia, CT is the gold standard for lung imaging in COVID-19 patients¹. However, CT imaging exposes the patient to a considerable amount of radiation, and is not as widely available as plain chest X-rays. Therefore, alternative low-dose imaging X-ray techniques are highly desirable. Here we present the first clinical results employing a novel dark-field chest X-ray imaging method for the assessment of COVID-19-pneumonia. The work is based on recent technological advancements in a human-scale X-ray dark-field chest imaging prototype that enable the acquisition of quantitative dark-field radiographs with diagnostic image quality at a radiation dose comparable to conventional X-rays². In a reader study, we found that dark-field imaging has a higher sensitivity for COVID-19-pneumonia than attenuation-based imaging, and that the combination of both is superior to one imaging modality alone. Furthermore, a quantitative image analysis showed a significant reduction of signal in X-ray dark-field chest radiographs of COVID-19 patients. While our results demonstrate that dark-field chest radiography presents an ultra-low-dose alternative to CT imaging for the assessment of COVID-19-pneumonia, we anticipate that the presented technique will also be useful for therapy follow-up of patients with long-COVID-syndrome³ and, more generally, for the imaging of other pulmonary pathologies.

The pandemic of severe acute respiratory syndrome coronavirus 2 (SARS-CoV-2) has led to a global medical, social, and economic crisis. The respective respiratory illness, coronavirus disease 2019 (COVID-19), has so far caused over six million deaths worldwide⁴.

At present, the reverse transcription-polymerase chain reaction (RT-PCR) test is the standard of reference for the definitive diagnosis of COVID-19^{5,6}. While the Fleischner Society recommends computed tomography (CT) imaging in patients with COVID-19 and worsening respiratory status under certain conditions⁷, the use of CT as primary screening tool is discouraged⁸. However, in daily clinical routine CT is often used to assess the extent of pulmonary changes associated with COVID-19. As chest CT is associated with a rather high radiation dose, alternative low-dose imaging techniques for the reliable evaluation and monitoring of pulmonary pathologies are highly desirable. This includes the potential application for follow-up assessment of patients suffering from long-COVID-syndrome, as radiation exposure reduction is crucial especially in the setting of repetitive scans.

Dark-field X-ray imaging⁹ has been proposed as a new diagnostic tool for the assessment of micro-structural changes in lung parenchyma and has been positively evaluated for the imaging of various lung diseases in mouse models¹⁰⁻¹² and first studies in humans^{13,14}. In contrast to conventional X-ray imaging, which utilizes the attenuation of X-rays in the specimen, X-ray dark-field contrast is generated by small-angle scattering of X-rays due to multiple refractions⁹. While the healthy lung consists of many refracting tissue-air-interfaces, generating a high dark-field signal, pulmonary disorders such as lung cancer, emphysema, fibrosis, or pneumonia decrease the dark-field signal by reducing the number of interfaces^{10,11,15,16}. Previous works have already shown the feasibility of upscaling from the mouse model to human dimensions with a radiation dose comparable to conventional X-rays^{2,13,14}. In this work, we describe several key advances of the dark-field chest X-ray imaging technique and its first application for the assessment of COVID-19-pneumonia in the human lung.

The Dark-field X-ray Prototype

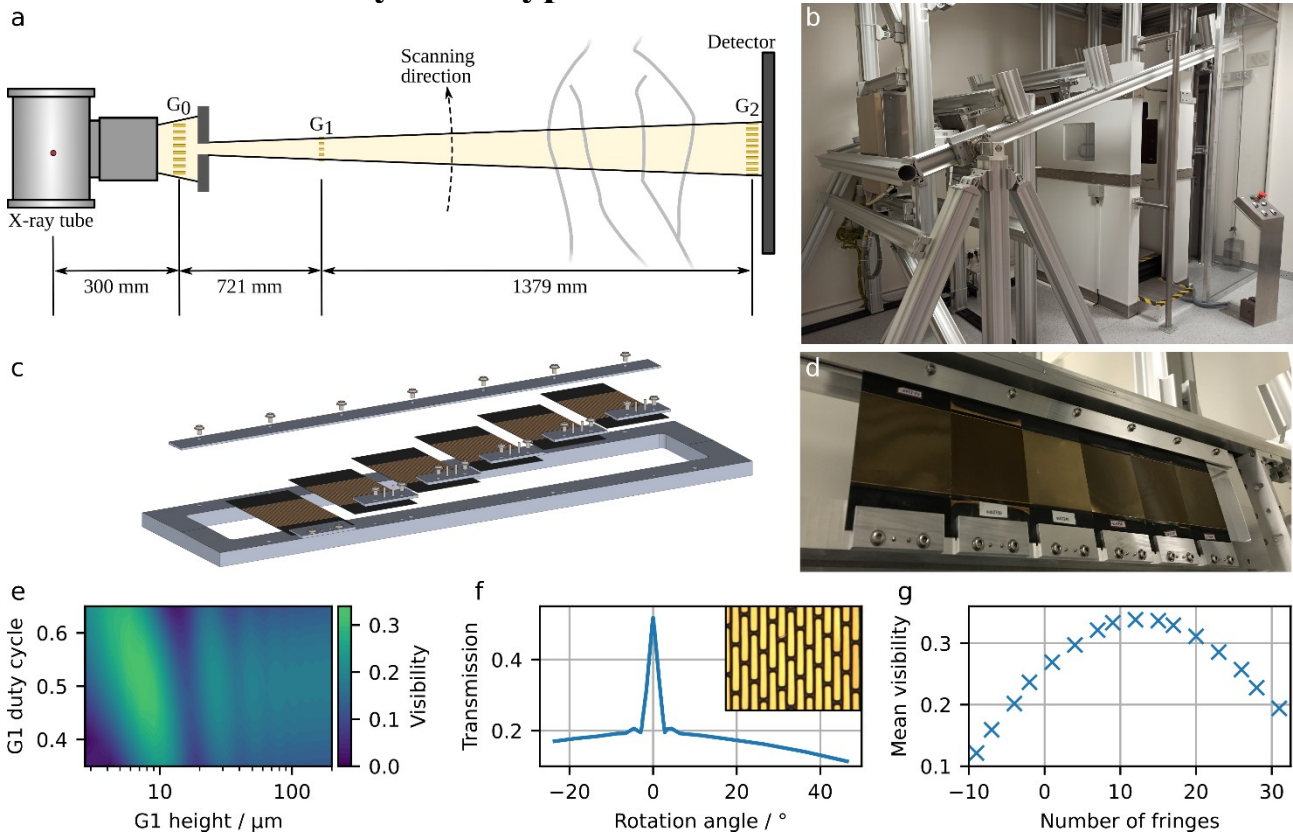


Figure 1 | Design and implementation of the dark-field chest X-ray prototype. *a*, Schematic and *b*, photograph of the prototype system, combining a conventional radiography setup with a three-grating X-ray interferometer. *c*, Schematic and *d*, photograph of the G2 grating holder allowing individual positioning of the gratings as well as bending of the gratings according to the cone-beam geometry. Bending prevents shadowing of the gold bars of the high aspect ratio gratings. *e*, Simulated visibility for optimising of grating parameters such as duty cycle and height. Optimisation was carried out iteratively for all three gratings. *f*, Angular X-ray transmission measurements and scanning electron microscopy image (inlet) for one of the grating structures. *g*, Influence of number of fringes per frame on mean interferometric visibility.

The first demonstrator system for clinical dark-field chest radiography in human patients consists of a conventional radiography system equipped with a three-grating X-ray interferometer^{13,14}. A schematic of the system and a photograph are shown in Figure 1a and Figure 1b. The interferometer enables the simultaneous acquisition of both conventional attenuation and novel dark-field X-ray images. A medical X-ray generator is suspended from the ceiling to decouple the vibrations due to its anode rotations from the interferometer. The patient is standing upright within the interferometer inside a patient cabin to prevent injury and damage to the interferometer. A conventional flat-panel detector is mounted behind the patient cabin and the gratings, enabling a field-of-view of about 37 cm x 37 cm in the patient plane.

This large-scale system posed challenges previously not encountered. As the production of large area absorbing gratings with a high-aspect ratio remains challenging, the analyser grating consists of six

separate tiles. To prevent shadowing resulting from the cone beam geometry of the setup¹⁷, we designed a grating holder that allows bending the gratings along the axis of their lamellae via dowel pins, as well as individual positioning of the tiles. Figure 1c and 1d depict a schematic and a photograph of the grating holder with its components, respectively.

Further, an in-depth optimisation of the gratings themselves is necessary for optimal performance of the interferometer. The interferometric visibility is a measure of contrast in the interference pattern generated by the gratings. A higher initial visibility results in a better SNR in the final dark-field image¹⁸, which is retrieved from the visibility reduction induced by small angle-scattering. Depending on setup-specific parameters such as length of the interferometer and X-ray spectrum, the grating parameters such as duty cycle and lamella height need to be adapted for maximum visibility. Therefore, a propagation and simulation framework for X-ray grating interferometers was created to optimize these grating parameters. An exemplary simulated visibility map for optimising G1 height and duty cycle can be found in Figure 1d. In an iterative process, parameters of all three gratings were optimised regarding obtained visibility and producibility.

Ensuring the uniformity of the gratings' duty cycle and lamella height are crucial for maximizing the visibility of the setup and thus image quality. The newly developed angular X-ray transmission¹⁹ (Figure 1f) allows for non-destructive and easily implementable parameter examination of gratings, and conventional SEM (Figure 1f, Inlet) was used for local and surface-based analysis.

The interferometric visibility also depends on the number of moiré fringes as depicted in Figure 1g. The change in fringe number is achieved by adjusting the exact position of the phase grating within the beam path. A certain number of moiré fringes is observed, because the grating periods do not exactly match the magnification condition of the cone beam geometry anymore. We found the highest visibility of 35 % for 11 fringes and chose this configuration for clinical operation (see Figure 2b).

Optimising Interferometer Performance

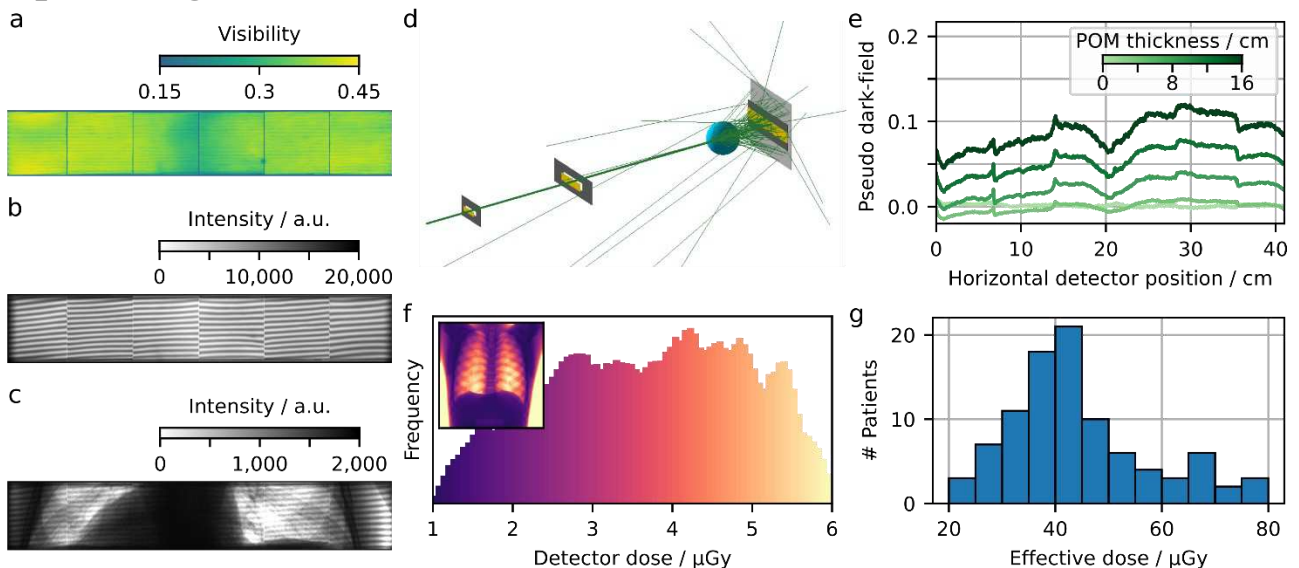


Figure 2 | Optimising the interferometer for the detection of pulmonary pathologies. *a*, Interferometric visibility map, which is a measure for the setup sensitivity. *b*, One exemplary raw image frame without and *c*, with a patient in the beam path. The changes in the interference pattern

induced by a sample allow for (conventional) attenuation- and (novel) dark-field image extraction. d, Monte-Carlo simulation of Compton scatter, adapted for setup specific parameters. Based on such simulations, a correction for Compton scatter induced dark-field contribution was applied. e, Beam hardening induced by an equivalent absorber material (here polyoxymethylene, POM). We implemented a beam hardening correction based on POM, assuming similar spectral behaviour between calibration material and patient. f, Dose histogram of the lung region and detector dose map of a thorax phantom (inlet). g, Histogram of effective dose deposited in the patients. For the patients described here, we report a mean (median) effective dose of 46.6 (47.1) μGy .

A uniform visibility in the field of view ensures a constant dark-field sampling range, as the dark-field corresponds to a loss of visibility induced by a sample. The interferometric visibility without a sample in the beam path amounts to approximately 35%, as depicted for one interferometer position in Figure 2a. The achieved visibility corresponds to the simulated visibility with the optimised grating parameters (cf. Figure 1e). An exemplary raw data frame without a sample in the beam path can be seen in Figure 2b. The moiré fringes, introduced by a small mismatch of the grating positions, are used to sample the intensity pattern with different relative grating positions when scanning the illuminated area over one pixel. Furthermore, the stitching gaps between the six grating tiles of the analyser grating subdivide the raw frame. By introducing a sample in the beam path, both the fringe pattern's mean intensity as well as its contrast can change. Figure 2c depicts the raw data of a frame taken from an exemplary patient scan. Absorbing features appear dark, while the scattering lung reduces the contrast of the fringe pattern.

As the measured visibility in a polychromatic setup is a weighted average of photon-energy-dependent visibility, an attenuating object changes the measured visibility due to spectrally varying attenuation, resulting in beam hardening artifacts in dark-field images²⁰. Figure 2e depicts horizontal profiles of the beam hardening induced change in visibility and therefore generated pseudo dark-field signal that occurs by introducing variant amounts of polyoxymethylene (POM) in the beam path. Due to inhomogeneities in the gratings as well as a variation of the source spectrum over the whole field of view, this effect depends on the spatial position on the detector. We see a strong dependence on the individual tiles of grating G2, with less pronounced changes in scanning direction (not in figure). We implemented a correction based on POM (aluminium), as its spectral absorption is similar to the one of soft tissue (bones). Using the approximation that the attenuation is caused by POM and aluminium in equal parts, we calculate the beam hardening induced dark-field signal pixelwise, and subtract it from the measured dark-field signal.

Another effect distorting the visibility signal is Compton scatter, as it superimposes the recorded intensity pattern resulting in a reduced contrast and therefore increased dark-field signal. A correction for Compton scatter induced dark-field signal is implemented, based on the measured attenuation and Monte-Carlo simulations that are adapted from the Skyflow Software (Royal Philips, The Netherlands)^{21,22} for setup-specific parameters. From the attenuation image, the distribution of material in the beam path, approximated as water only, is estimated. The intensity at the detector due to scatter is then calculated from the material distribution using scattering kernels, determined previously by Monte-Carlo simulations taking into account the spectrum and the setup geometry. An exemplary Compton scatter simulation is shown in Figure 2d.

Within the approval process of the demonstrator system, clinical safety measures such as patient exposure and automatic shut-off to prevent overexposure were validated. An anthropomorphic thorax phantom was used for evaluating the detector dose in the examined lung (cf. Figure 2f, Inlet depicts dose image of the whole field-of-view). The target detector dose was chosen such that the effective dose of the reference person amounts to 35 μSv for one scan in posterior-anterior orientation². The so obtained dose values (Figure 2g) for examined patients range from about 20–80 μSv , depending mainly on the patient's weight, with a mean value of 46.6 μSv and a median of 41.7 μSv , which is within reported chest radiography values²³.

COVID-19 in Dark-field Chest X-rays

Image appearance

A total of 100 patients (56 men, 44 women) were included, of which 40 were healthy controls and 60 had COVID-19-pneumonia. The average age of the subjects was 58.75 ± 14.01 years.

Figure 3 shows the first X-ray dark-field imaging results on COVID-19 patients and healthy controls. Compared to dark-field images in healthy subjects, those in patients with typical COVID-19-pneumonia in the CT scan showed an overall decrease of the dark-field signal. While dark-field images in healthy subjects exhibit a rather homogeneous structure¹³, images of COVID-19 patients appear rather inhomogeneous and patchy, especially in the lung periphery, corresponding well to ground glass opacities in the respective CT scan (cf. Supplementary Figure 1). While changes are obvious in dark-field images, conventional X-ray images of healthy subjects and infected patients are difficult to distinguish.

0.0 Dark-field signal 0.8

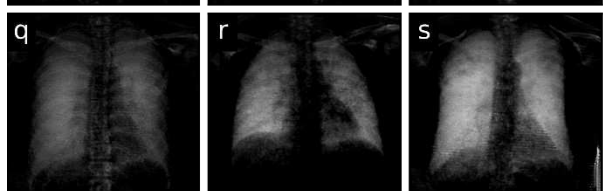
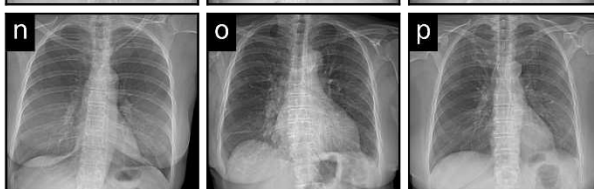
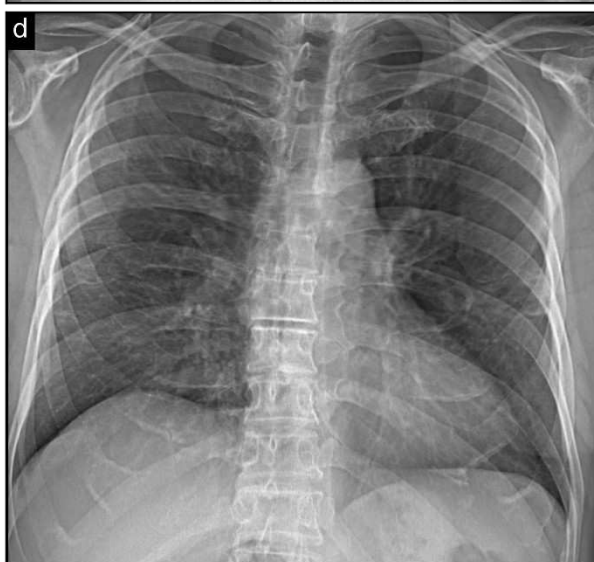
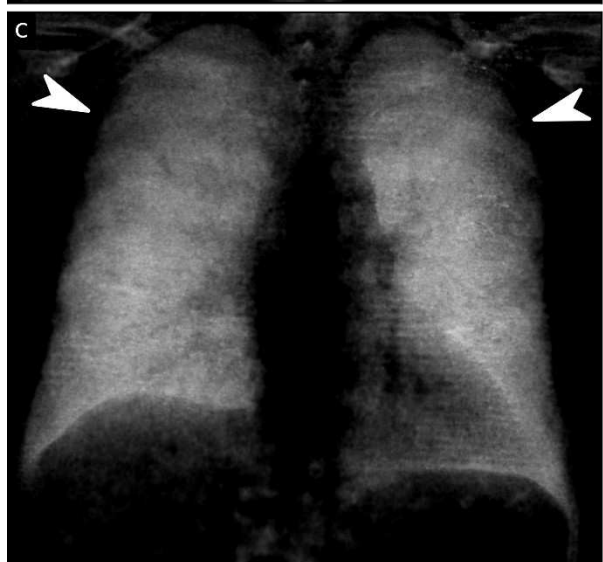
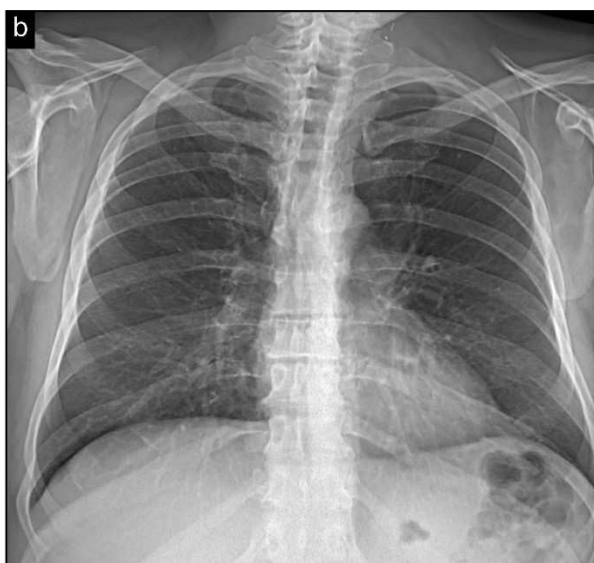


Figure 3 | Dark-field and conventional chest X-rays of healthy and COVID-19-infected subjects. *a*, Dark-field and *b*, conventional (attenuation-based) chest radiographs of a healthy subject. The dark-field radiograph exhibits a strong, homogeneous dark-field signal. The respective attenuation-based image shows no apparent pathology. *c*, Dark-field and *d*, attenuation-based chest radiographs of a patient infected with COVID-19. Compared to the healthy subject, the infected patient shows an overall decrease of signal intensity. While the signal of the healthy subject is homogeneous, the dark-field signal of the infected patient appears inhomogeneous and patchy, especially in the periphery of the lung (arrowheads). *e-g*, Additional exemplary dark-field radiographs of healthy subjects, *h-j*, respective attenuation-based radiographs. *k-v*, More exemplary dark-field and respective attenuation-based images of patients infected with COVID-19. *k-m*, Dark-field images with a generally reduced signal intensity. *q-r*, Dark-field images with a rather inhomogeneous, patchy texture, predominantly in the periphery. *n-p*, and *t-v*, respective attenuation-based images in comparison, in which it is rather difficult to impossible to detect COVID-19-pneumonia.

Reader Study and Quantitative Analysis

To evaluate the potential clinical impact, we performed a reader study for the detection of COVID-19-pneumonia on both attenuation-based and dark-field images alone, as well as both images displayed simultaneously. The ratings for the presence of COVID-19-pneumonia in healthy subjects and patients with COVID-19-pneumonia in the CT scan did show a highly significant difference for all displayed variations, attenuation-based, dark-field-based imaging, and the combination of both ($p < 0.05$ for all) (Figure 4a). Overall rating values for the presence of COVID-19-pneumonia in infected patients were substantially higher for dark-field imaging (4.84 ± 1.39) compared to attenuation-based imaging (3.16 ± 1.46). Additionally, rating values for infected patients were higher for the combination of dark-field-based and (conventional) attenuation-based imaging (5.04 ± 1.37) compared to dark-field based imaging alone. In a receiver operating characteristic (ROC) analysis for the differentiation between infected patients and healthy subjects, the effect size expressed as the area under the ROC curve (AUC) was 0.78 (95% confidence interval (CI) 0.73 to 0.83) for attenuation-based radiographs, 0.91 (95% CI 0.88 to 0.94) for dark-field images and 0.93 (95% CI 0.91 to 0.96) for the combination of both (Figure 4b). By including dark-field images, AUC values were significantly higher compared to attenuation images only ($p = 3.9e-6$ for dark-field alone, $p = 3.5e-9$ for combination).

For comparison, we additionally applied the winning neural network of the SIIM-FISABIO-RSNA COVID-19 Detection Challenge²⁴, trained on conventional attenuation images, to the attenuation images of both the COVID-19 patients and healthy controls. In this setting, an AUC value of 0.88 was achieved, which can also be found in literature²⁵. This value was higher than the AUC achieved by readers on the same images. However, compared to the trained network, readers achieved an even higher AUC when reading dark-field images alone or the combination of both imaging modalities (Figure 4b).

The overall sensitivity for COVID-19-pneumonia was 0.43 (95% CI 0.38 to 0.48) for attenuation-based images, 0.86 (95% CI 0.80 to 0.92) for dark-field images, and 0.88 (95% CI 0.82 to 0.94) for the combination of both. Respective specificities and accuracies, also on individual reader basis, are shown in Supplementary Table 1. The inter-rater reliability between the readers ranged 0.16 – 0.42 for attenuation-based imaging, 0.56 – 0.67 for dark-field imaging, and 0.48 – 0.74 for the

combination of both. Reader-specific reliability scores are provided in Supplementary Table 2. The average rating of image quality over all readers was 4.97 ± 0.99 for dark-field and 5.35 ± 0.66 for attenuation-based imaging.

For a quantitative analysis of the dark-field signal, we calculated the average dark-field coefficient of every patient's lung, corresponding to the average dark-field signal generated per path length through the lung parenchyma¹³. The average dark-field coefficient was significantly lower in patients infected with COVID-19 ($2.15 \pm 0.44 \text{ m}^{-1}$) compared to healthy subjects ($2.53 \pm 0.44 \text{ m}^{-1}$, $p = 8.6\text{e-}5$), as depicted in Figure 4c.

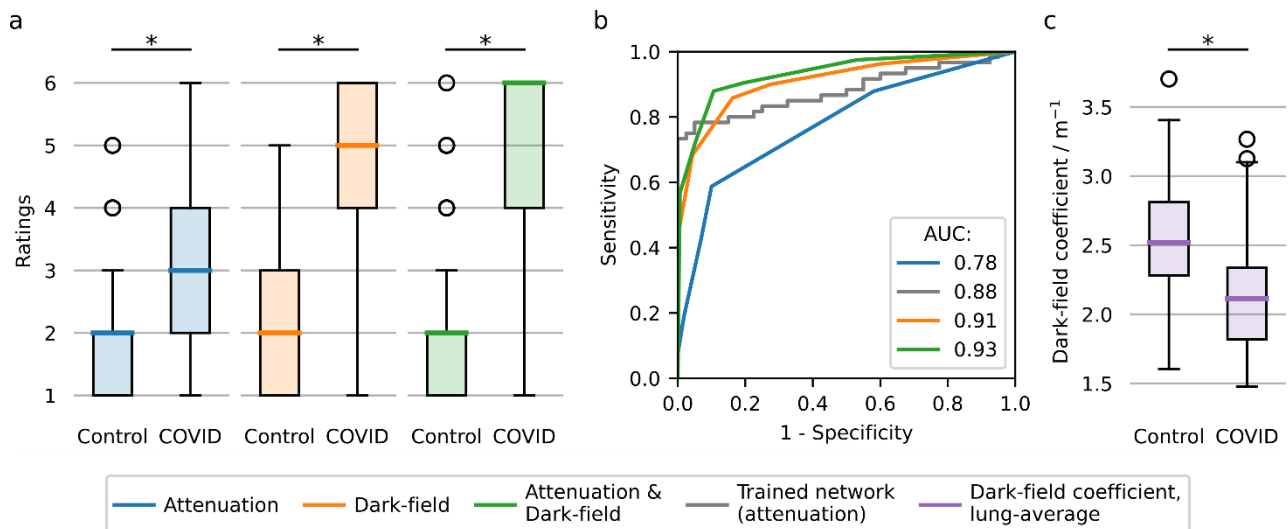


Figure 4 | Results of clinical evaluation and statistical analysis. *a*, Reader scores for both healthy subjects and infected patients in dark-field-based, attenuation-based, and dark-field- & attenuation-based readings. *b*, Receiver operator characteristic (ROC) analysis for the respective modalities for the differentiation between infected patients and healthy subjects. Additionally, an AI algorithm (convolutional neural network) for COVID-19 pneumonia detection was applied for attenuation image evaluation. Area under the curve (AUC) values were 0.78 (attenuation), 0.88 (trained network on attenuation), 0.91 (dark-field), and 0.93 (dark-field & attenuation), respectively. *c*, Objective, quantitative image analysis, showing the average dark-field coefficient (integrated over the whole lung area and evaluated after segmentation) for the lungs of healthy subjects and infected patients. Significant differences are indicated by asterisks: *, $p < 0.05$. Abbreviations; AUC, area under the curve.

Discussion

In this study we present the first application of the recently developed dark-field X-ray imaging technology for the assessment of COVID-19-pneumonia and demonstrate its superiority over conventional radiography. This essentially introduces a low-radiation, medical imaging alternative to present CT imaging for COVID-19-pneumonia detection and therapy follow-up. Along with detailed subjective and objective clinical evaluation results, we also present some of the key technological improvements, which were necessary to optimise the system for imaging of pulmonary pathologies such as COVID-19-associated lung changes.

While we have achieved promising first results, some limitations of our approach and study exist. On the technological side, it first has to be noted that due to the restricted available grating sizes, the setup was realised as a slot scanning system. While this compromise allowed the first realisation of a clinical dark-field radiography study on COVID-19-pneumonia, future hardware improvements, such as the fabrication of full-field gratings, could enhance the current realization by eliminating the scanning procedure and thus simplifying the setup. Gratings with larger aspect ratios could increase the interferometric visibility, leading to a higher signal-to-noise ratio in dark-field images or lower effective doses. Also, gratings with smaller periods would increase the sensitivity of the setup, enabling the use of higher tube voltages and thus further decrease the effective patient dose.

From a more clinical perspective, we showed that X-ray dark-field chest imaging is a fast, low-dose technique that yields both a conventional attenuation image and a novel, complementary dark-field image. It allows for the reliable detection of COVID-19-pneumonia and is in that respect superior to conventional radiography. For the latter, our results are in line with a previous study by Self et al.²⁶, who found a similar sensitivity for the detection of pulmonary opacities in conventional attenuation radiographs as we found for attenuation images alone. In the performed reader study, the simultaneous presentation of both attenuation images and dark-field images yielded an even higher sensitivity compared to each imaging technique individually. The combined information from both attenuation and dark-field images provides an even better picture of the ventilation situation of the lung, also reflected by the higher inter-rater reliability for the combination of both imaging modalities compared to each imaging modality separately. Even though the achieved sensitivity when reading both modalities is not as high as in CT imaging²⁶, it is still reasonably high and comes with only a fraction of the dose. We included only patients with moderate courses of the disease that were able to stand upright and hold breath for the duration of the scan. These patients could be clearly distinguished from healthy controls, underlining the potential of the technique to detect even minor lung changes such as ground glass opacities.

While the evaluation of attenuation images was enhanced by a trained neural network, the reader-based assessment of dark-field images outperforms the algorithm. Finally, we are confident that there is potential to further enhance these results by applying artificial intelligence on dark-field images once a sufficiently large number of cases is available for training.

The patient study also exhibits some limitations. The study cohort, comprising 100 subjects, is presently relatively small and the technique must be further evaluated in future studies with larger cohorts. In this context, another drawback is also that potential pulmonary comorbidities in COVID-19 patients are not taken into account, while the control group comprised only healthy subjects without any pulmonary disorders. While this initial pilot study aimed at evaluating the accuracy of X-ray dark-field imaging for the detection of COVID-19-pneumonia compared to pulmonary healthy subjects, future studies must be performed to evaluate the technique for the assessment of the lung when other pathologies are present.

Moreover, as the average dark-field coefficient is a measure for the alveolar integrity, it decreases with the presence of COVID-19-pneumonia. Currently, no pixel-based analysis is available, as the projected lung thickness in each pixel, which is necessary for normalization of the dark-field signal with the respective lung thickness, remains unknown. Therefore, only the average dark-field coefficient of the whole lung is available as the total signal is normalised with the lung volume. This leads to only a small reduction of the average dark-field coefficient in the presence of beginning and localised pneumonia, while the dark-field images show a distinct localised signal decrease in these cases. Whereas the quantitative analysis does not allow for the assessment of local changes in dark-field signal, radiologists may detect patterns of local signal losses. Future studies are needed to analyse the dark-field signal locally and therefore allow for a quantitative assessment of the alveolar integrity on a pixel-basis.

While further technological improvements might enable a more accurate assessment of pulmonary pathologies in the future, more clinical studies are needed to evaluate the technique's potential for lung imaging. Dark-field imaging might, for example, also be suitable for disease and treatment monitoring of COVID-19 patients due to the obtained image-based information on the lung's alveolar condition at a low effective patient dose. With constantly new variants increasingly leading to higher infection rates²⁷ and severe courses in younger patients²⁸, dark-field imaging might be a low-radiation alternative for disease monitoring especially in patients where repetitive CT scans should be avoided. Low-dose imaging techniques such as dark-field radiography are also highly desirable for the assessment of pulmonary involvement in patients with long-COVID-syndrome. However, this potential use case of the presented technique is yet to be evaluated. Nevertheless, the presented study highlights the potential of dark-field chest X-ray imaging for the assessment of COVID-19-pneumonia and shows that it might therefore be a promising new tool in the fight against the SARS-CoV-2 pandemic.

Methods

Hardware

The X-ray tube (MRC 200 0508, Royal Philips, The Netherlands) is operated at 70 kV in a pulsed mode at a frame rate of 30 Hz. The tube voltage was chosen because the most favourable combination of image quality, signal strength, and sharpness is present at 70 kV in both dark-field and attenuation images²⁹. Tube current is adapted to each patient via his or her body mass index (BMI), as a high correlation between BMI and necessary tube current was found in a first patient study. The flat-panel detector (Pixium FE 4343, Trixell, France) simultaneously acquires images at a time window of about 17 ms per frame. One scan consists of a maximum of 195 single frames taken in about 7 s. An additional mobile collimator (2 mm tungsten) is fixed to the source grating G0, limiting the actively irradiated area to the gratings, further reducing patient exposure. Downstream both collimators, an ionisation chamber (Diamentor CI, PTW, Germany) captures the entire radiation area to record the applied radiation dose of each scan. The effective patient dose is estimated from the measured dose area product (DAP)².

Clinical Image Acquisition

As both X-ray tube and detector are stationary, the patient is positioned within the beam path via a lifting platform inside of the patient cabin. Both the positioning of the lifting platform and the movement of the interferometer can be operated with the control panel, located outside of the patient cabin. The shutters for vertical and horizontal collimation are also adjusted from there. The scan is triggered from the control room and automatic breathing instructions are given. All images were acquired in full inspiration.

Image Reconstruction

Dark-field radiography with a three grating Talbot-Lau interferometer works by analysing the fringe pattern produced by the phase grating G1 and sampled by the analyser grating G2. The source grating G0 is necessary to assure spatial coherence from a polychromatic X-ray source³⁰. As the fringe pattern is too fine to be resolved by a conventional flat-panel detector, a slight mismatch in grating alignment is introduced to create moire fringes on a resolvable scale for scanning image acquisition. By scanning the moire fringes across the sample, a varying intensity is registered in every pixel for each image frame^{31,32}. The so-called stepping curve can be extracted by a least-squares fit of a sinusoidal intensity model to the recorded intensities⁹. Additionally, scanning allows to expand the FOV into one direction, enabling the coverage of a human thorax. The difference between patient scan and reference scan in the recorded intensities allows extraction of the attenuation and the dark-field image³³. The high scanning speed introduces mechanical vibrations and therefore misalignment of the gratings, which we estimate with a maximum-likelihood method. Still, the acquisition time is increased compared to conventional chest radiography, resulting in motion artifacts especially around the heart contour and the aortic arch. By artificially narrowing the slot and reducing the number of frames for image extraction in affected areas, these motion artifacts can be strongly reduced³⁴.

Patient recruitment

Patients

Institutional Review Board (IRB) and national radiation protection agency approval (*REFERENCE NUMBER BLINDED FOR REVIEW*) was obtained prior to this study (*IRB AND REFERENCE NUMBER BLINDED FOR REVIEW*). Patients gave their written informed consent prior to study participation.

COVID-19 patients

Between May 2020 and December 2020, patients of legal age that underwent chest CT at our institution as part of their diagnostic workup and a clinically suspected COVID-19 infection were screened for study participation. All CT images of potential study participants were analysed for COVID-19-pneumonia by two of three radiologists (*BLINDED FOR REVIEW* with 2, 6, and 12 years of experience in chest CT imaging) immediately after the scan according to the CO-RADS assessment scheme for patients suspected of having COVID-19³⁵.

Only patients with a CO-RADS category 4 (suspicious for COVID-19), 5 (typical for COVID-19), or 6 (RT-PCR positive for SARS-CoV-2, if patients had been tested before the CT scan) were included in this study. Other inclusion criteria were the ability to consent, to stand upright without help, and to hold breath for 7 seconds. Eligible patients were approached right after the CT scan.

Exclusion criteria were a negative RT-PCR test within 2 days before the CT scan, pregnancy, lung cancer, and pneumothorax. 60 patients with suspected COVID-19 infection were included in this study.

Controls

Between October 2018 and January 2020, patients of legal age that underwent chest CT at our institution as part of their diagnostic workup were screened for study participation. All CT images of potential study participants were analysed for pathologic lung changes by three radiologists (*BLINDED FOR REVIEW* with 2, 6, and 12 years of experience in chest CT imaging). Inclusion criteria were a normal chest CT scan, the ability to consent, to stand upright without help, and to hold breath for 7 seconds. Eligible patients were approached right after the CT scan. Exclusion criteria were pregnancy, strong medical conditions, and changes in the lung tissue such as cancer, pleural effusion, atelectasis, emphysema, infiltrates, ground glass opacities, and pneumothorax. 40 patients were included in the control group, previously reported by Gassert et al.¹³.

CT

CT was performed on one of three CT scanners (Philips iCT, Siemens SOMATOM, and Philips IQon Spectral CT) with the following parameters, according to routine clinical protocols: Reconstructed slice thickness, 0.625-0.9 mm; pixel spacing, 0.4/0.3 mm; pitch factor, 0.8/0.9; tube voltage (peak), 120 kV; modulated tube current, 125–350 mAs. Images were reformatted in 3 mm slice thickness using a lung-specific kernel.

Image Evaluation

Four radiologists (*BLINDED FOR REVIEW*) with different levels of experience in dark-field imaging (2, 5, 7, 9 years) assessed only attenuation-based radiographs, only dark-field radiographs, and both displayed simultaneously for all patients. All readers were blinded to the group affiliation of images and images were presented in a random order. Readers used a PACS system and authorised monitors used in everyday clinical practice and were asked to rate the presence of COVID-19-pneumonia on a scale from 1 to 6 (1 = surely not, 2 = very unlikely, 3 = unlikely, 4 = likely, 5 = very likely, 6 = surely). Window settings were optimised for image illustration with the same window level for all images within each modality. Readers were allowed to adjust window levels at their convenience. Values 1 to 3 were counted as negatives, while values 4 to 6 were counted as positives. Attenuation-based images were additionally evaluated by using the winning neural network of the SIIM-FISABIO-RSNA COVID-19 Detection Challenge²⁴, which provides a probability for the presence of COVID-19-pneumonia for each patient.

The quantitative dark-field coefficient was calculated according to Gassert et al.¹³.

Statistical Analysis

Statistical analysis was performed with Python (version 3.8.5), specifically using the packages NumPy (version 1.20.2)³⁶ and SciPy (version 1.5.4)³⁷, as well as R (version 4.1.1) for the receiver operating characteristic (ROC) analysis. The area under the ROC curve (AUC) was calculated for all three reading modalities and AUC values were tested for differences with Obuchowski's method for correlated and clustered ROC data³⁸. Additionally, a z-test based on AUC values was used to determine whether the ratings of the two groups (healthy subjects and patients with COVID-19-pneumonia) differ within each reading modality. The averaged dark-field coefficients were tested for normal distribution using the Shapiro-Wilk-test and only the coefficient of the healthy subjects was found to follow a normal distribution. Therefore, a two-sided Mann-Whitney-U-test was applied to determine whether the two groups (healthy subjects and patients with COVID-19-pneumonia) differ in averaged dark-field coefficient. For all tests, a 0.05 level of significance was chosen. The inter-reader reliability for the presence of COVID-19-pneumonia was rated with Cohen's weighted kappa (with quadratic weights).

References

1. Guan, W. *et al.* Clinical Characteristics of Coronavirus Disease 2019 in China. *N. Engl. J. Med.* **382**, 1708–1720 (2020).
2. Frank, M. *et al.* Dosimetry on first clinical dark-field chest radiography. *Med. Phys.* **48**, 6152–6159 (2021).
3. Mahase, E. Covid-19: What do we know about ‘long covid’? *BMJ* **370**, 9–10 (2020).
4. Johns Hopkins University. COVID-19 Dashboard. Available at: <https://gisanddata.maps.arcgis.com/apps/dashboards/bda7594740fd40299423467b48e9ecf6>. (Accessed: 7th March 2022)
5. Li, Q. *et al.* Early Transmission Dynamics in Wuhan, China, of Novel Coronavirus–Infected Pneumonia. *N. Engl. J. Med.* **382**, 1199–1207 (2020).
6. Chen, N. *et al.* Epidemiological and clinical characteristics of 99 cases of 2019 novel coronavirus pneumonia in Wuhan, China: a descriptive study. *Lancet* **395**, 507–513 (2020).
7. Rubin, G. D. *et al.* The Role of Chest Imaging in Patient Management During the COVID-19 Pandemic: A Multinational Consensus Statement From the Fleischner Society. *Chest* **158**, 106–116 (2020).
8. Raptis, C. A. *et al.* Chest CT and Coronavirus Disease (COVID-19): A Critical Review of the Literature to Date. *Am. J. Roentgenol.* **215**, 839–842 (2020).
9. Pfeiffer, F. *et al.* Hard-X-ray dark-field imaging using a grating interferometer. *Nat. Mater.* **7**, 134–137 (2008).
10. Hellbach, K. *et al.* In vivo dark-field radiography for early diagnosis and staging of pulmonary emphysema. *Invest. Radiol.* **50**, 430–435 (2015).
11. Yaroshenko, A. *et al.* Improved in vivo Assessment of Pulmonary Fibrosis in Mice using X-Ray Dark-Field Radiography. *Sci. Rep.* **5**, (2015).
12. Meinel, F. G. *et al.* Diagnosing and Mapping Pulmonary Emphysema on X-Ray Projection Images: Incremental Value of Grating-Based X-Ray Dark-Field Imaging. *PLoS One* **8**, (2013).
13. Gassert, F. T. *et al.* X-ray Dark-Field Chest Imaging: Qualitative and Quantitative Results in Healthy Humans. *Radiology* **301**, 389–395 (2021).
14. Willer, K. *et al.* X-ray dark-field chest imaging for detection and quantification of emphysema in patients with chronic obstructive pulmonary disease: a diagnostic accuracy study. *Lancet Digit. Heal.* **3**, e733–e744 (2021).
15. Scherer, K. *et al.* X-ray Dark-field Radiography - In-Vivo Diagnosis of Lung Cancer in Mice. *Sci. Rep.* **7**, 402 (2017).
16. Hellbach, K. *et al.* X-Ray Dark-field Imaging to Depict Acute Lung Inflammation in Mice. *Sci. Rep.* **8**, 2096 (2018).
17. Kageyama, M. *et al.* X-ray phase-imaging scanner with tiled bent gratings for large-field-of-view nondestructive testing. *NDT E Int.* **105**, 19–24 (2019).
18. Chabior, M. *et al.* Signal-to-noise ratio in x ray dark-field imaging using a grating interferometer. *J. Appl. Phys.* **110**, (2011).
19. Gustschin, N. *et al.* Quality and parameter control of X-ray absorption gratings by angular X-ray transmission. *Opt. Express* **27**, 15943 (2019).
20. Yashiro, W., Vagovič, P. & Momose, A. Effect of beam hardening on a visibility-contrast image obtained by X-ray grating interferometry. *Opt. Express* **23**, 23462 (2015).
21. Bertram, M., Hohmann, S. & Wiegert, J. SU-FF-I-22: Scatter Correction for Flat Detector Cone-Beam CT Based On Simulated Sphere Models. *Med. Phys.* **34**, 2342–2343 (2007).
22. Mentrup, D., Jockel, S., Menser, B. & Neitzel, U. Iterative scatter correction for grid-less bedside chest radiography: Performance for a chest phantom. *Radiat. Prot. Dosimetry* **169**,

- 308–312 (2016).
23. Mettler, F. A., Huda, W., Yoshizumi, T. T. & Mahesh, M. Effective doses in radiology and diagnostic nuclear medicine: A catalog. *Radiology* **248**, 254–263 (2008).
 24. Lakhani, P. *et al.* The 2021 SIIM-FISABIO-RSNA Machine Learning COVID-19 Challenge: Annotation and Standard Exam Classification of COVID-19 Chest Radiographs. (2021).
 25. Hurt, B. *et al.* Radiologist-supervised Transfer Learning. *J. Thorac. Imaging Publish Ah*, (2021).
 26. Self, W. H., Courtney, D. M., McNaughton, C. D., Wunderink, R. G. & Kline, J. A. High discordance of chest x-ray and computed tomography for detection of pulmonary opacities in ED patients: Implications for diagnosing pneumonia. *Am. J. Emerg. Med.* **31**, 401–405 (2013).
 27. Mahase, E. Covid-19: Where are we on vaccines and variants? *BMJ* **372**, n597 (2021).
 28. Taylor, L. Covid-19: Brazil’s spiralling crisis is increasingly affecting young people. *BMJ* **373**, n879 (2021).
 29. Sauter, A. P. *et al.* Correlation of image quality parameters with tube voltage in X-ray dark-field chest radiography: a phantom study. *Sci. Rep.* **11**, 14130 (2021).
 30. Pfeiffer, F., Weitkamp, T., Bunk, O. & David, C. Phase retrieval and differential phase-contrast imaging with low-brilliance X-ray sources. *Nat. Phys.* **2**, 258–261 (2006).
 31. Koehler, T. *et al.* Slit-scanning differential x-ray phase-contrast mammography: Proof-of-concept experimental studies. *Med. Phys.* **42**, 1959–1965 (2015).
 32. Kottler, C., Pfeiffer, F., Bunk, O., Grünzweig, C. & David, C. Grating interferometer based scanning setup for hard x-ray phase contrast imaging. *Rev. Sci. Instrum.* **78**, 1–4 (2007).
 33. Pfeiffer, F. *et al.* X-ray dark-field and phase-contrast imaging using a grating interferometer. *J. Appl. Phys.* **105**, (2009).
 34. Schick, R. C. *et al.* Correction of Motion Artifacts in Dark-Field Radiography of the Human Chest. *IEEE Trans. Med. Imaging* 1–1 (2021). doi:10.1109/TMI.2021.3126492
 35. Prokop, M. *et al.* CO-RADS: A Categorical CT Assessment Scheme for Patients Suspected of Having COVID-19—Definition and Evaluation. *Radiology* **296**, E97–E104 (2020).
 36. Harris, C. R. *et al.* Array programming with NumPy. *Nature* **585**, 357–362 (2020).
 37. Virtanen, P. *et al.* SciPy 1.0: fundamental algorithms for scientific computing in Python. *Nat. Methods* **17**, 261–272 (2020).
 38. Obuchowski, N. A. Nonparametric Analysis of Clustered ROC Curve Data. *Biometrics* **53**, 567 (1997).

Acknowledgements

We acknowledge gratefully Felix Gebser, David Jany, Jens von Berg, Michael Heider, Karsten Rindt, Hendrik van der Heijden, Andre Braunagel, Jens von Berg, Pascal Meyer, and Jürgen Mohr for assistance during the hardware-and software-development for the demonstrator system, and Felix Meurer, Jannis Bodden, Yannik Leonhardt, Christina Müller-Leisse, Martin Renz, Nadja Meissner, and Angelika Kammermayer for help with patient handling, and Dung Nguyen Ba for providing us with the checkpoint weights for the inference models.

Additionally, we acknowledge financial support through the European Research Council (AdG 695045), the Deutsche Forschungsgemeinschaft (DFG, Research Training Group GRK 2274), the Federal Ministry of Education and Research (BMBF), and the Free State of Bavaria under the Excellence Strategy of the Federal Government and the Länder, as well as by the Technical University of Munich – Institute for Advanced Study. This work was carried out with the support of the Karlsruhe Nano Micro Facility (KNMF, www.kit.edu/knmf), a Helmholtz Research Infrastructure at Karlsruhe Institute of Technology (KIT).

Author Contributions

M.F., T.U., K.W., W.N., R.S., B.G., F.D.M., T.K., K.J.E., B.R., J.H., and F.P. developed hardware and control software of the demonstrator system. M.V. developed the visibility simulation for optimization of grating parameters. M.F., T.U., K.W., W.N., R.S., F.D.M., T.K., J.H., and F.P. developed the data processing algorithms. M.F. and M.S. adapted the neural network pipeline for the comparison of the attenuation images. F.T.G., F.G.G., A.A.F., A.P.S., and D.P. recruited patients and performed radiological interpretation of imaging data. M.F., F.T.G., and B.H. performed the statistical analysis. J.H., D.P., M.M., and F.P. supervised the project. M.F. and F.T.G. wrote the original draft and revised the manuscript with input from all authors. All authors approved the manuscript.

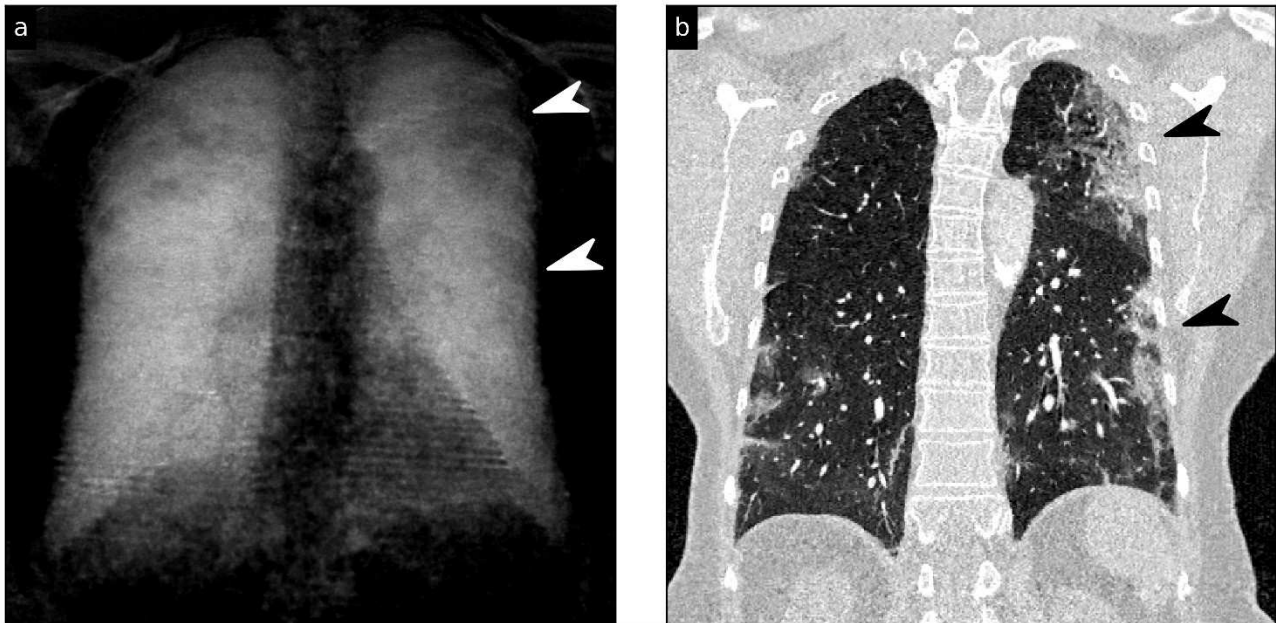
Competing interest's declaration

T.K. and K.J.E. are employees of Philips GmbH Innovative Technologies. The remaining authors declare no competing interests.

Data and materials availability

Underlying data and source code used in the evaluation of this study can be provided without patient identification upon reasonable request to researchers affiliated to accredited research institutions after entering a signed data access agreement. Proposals are required to address scientific questions and will be reviewed individually. Please direct your request to manuela.frank@tum.de.

Extended Material



Supplementary Figure 1 | Comparison of Dark-field chest X-ray and CT information for a selected patient. *a*, Dark-field chest X-ray radiograph and *b*, exemplary coronal CT slice of a 67-year-old female patient infected with COVID-19. The dark-field chest X-ray shows an overall signal reduction and an inhomogeneous structure. The patchy appearance in the periphery in the dark-field image corresponds well to the ground glass opacities and consolidated areas in the CT scan (arrowheads).

	Reader	Sensitivity	Specificity	Accuracy
Attenuation	1	0.50	0.84	0.63
	2	0.33	0.98	0.59
	3	0.38	1.00	0.63
	4	0.48	0.98	0.68
	Overall	0.43	0.93	0.63
Dark-field	1	0.92	0.95	0.93
	2	0.95	0.90	0.93
	3	0.92	0.88	0.90
	4	0.65	0.78	0.70
	Overall	0.86	0.84	0.85
Attenuation & Dark-field	1	0.93	0.97	0.95
	2	0.90	0.95	0.92
	3	0.88	0.95	0.91
	4	0.80	0.86	0.82
	Overall	0.88	0.89	0.89

Supplementary Table 1 | Sensitivity, specificity, and accuracy for each reader individually and overall.

Manuscript Draft: Confidential

	Attenuation	Dark-field	Attenuation & Dark-field
Reader 1 & Reader 2	0.27	0.56	0.48
Reader 1 & Reader 3	0.38	0.67	0.63
Reader 1 & Reader 4	0.36	0.57	0.59
Reader 2 & Reader 3	0.16	0.62	0.74
Reader 2 & Reader 4	0.22	0.65	0.66
Reader 3 & Reader 4	0.42	0.66	0.74

Supplementary Table 2 | Inter-rater reliability expressed with Cohen's quadratic weighted kappa.